

## Supporting Information

### Self-assembly of Ruthenium-doped Oxygen-deficient Tungsten Oxide as an Efficient Electrocatalyst for Hydrogen Evolution Reaction in Acidic Environments

Elhussein Desoki Helal<sup>a,b,#</sup>, Wenhai Xu<sup>a,#</sup>, Yizhe Li<sup>a</sup>, Liyao Gao<sup>a</sup>, Hao Sun<sup>a</sup>, Qingzhen Xu<sup>a</sup>, Imran Ali Chandio<sup>a</sup>, Safdar Abbas<sup>a</sup>, Abdul Hameed Pato<sup>a</sup>, Wen Liu<sup>\*a</sup>

<sup>a</sup>*State Key Laboratory of Chemical Resource Engineering, College of Chemistry, Beijing University of Chemical Technology, Beijing, 100092, China*

<sup>b</sup>*Chemistry Department, Faculty of Science, Benha University, Benha, 13518, Egypt*

<sup>#</sup> *These authors contributed equally to this work.*

## 1. Experimental sections:

### 1.1. Chemicals and materials

Tungsten (VI) chloride ( $\text{WCl}_6$ , 99.9%) and ruthenium (III) chloride hexahydrate ( $\text{RuCl}_3 \cdot 6\text{H}_2\text{O}$ , 99.9%) were all purchased from Aladdin Biological Technology Co., Ltd. Ethanol (99.9%), and a 5 wt% Nafion solution were purchased from Sigma-Aldrich. The carbon fiber paper (TGP-H-060) was purchased from Toray Industries, Inc., and the sulfuric acid ( $\text{H}_2\text{SO}_4$ , 98%) was purchased from Beijing Chemical Works. The 5 wt.%-Ru/C and 20 wt.%-Pt/C material were purchased from Adamas Chemical Reagent Co. Ltd. All the reagents were utilized directly without any further purification. All aqueous solutions were prepared using deionized water, which had a resistivity of  $18.2 \text{ M}\Omega \text{ cm}^{-1}$ .

### 1.2. Synthesis of Ru-doped $\text{W}_{18}\text{O}_{49}$ electrocatalysts

In the typical synthesis of urchin-like Ru-doped  $\text{W}_{18}\text{O}_{49}$ -5% nanospheres, 0.25 g of  $\text{WCl}_6$  (0.630 mmol) were added into 80 ml of absolute ethanol into a 100 ml Teflon vessel. The mixture was placed for continuously magnetic stirring for 30 minutes at room temperature till a clear yellow solution was formed. To this solution, 0.013 g (0.04 mmol) of  $\text{RuCl}_3 \cdot 6\text{H}_2\text{O}$  was added and the magnetic stirring continued for another 15 minutes. Then, it was transferred to an air oven and heated at  $180 \text{ }^\circ\text{C}$  for a period of 24 h. After the reaction was completed, it was naturally cooled to the room temperature. Then, the resultant product was collected by centrifugation at 4000 rpm for 5 minutes, and washed several times with ethanol and distilled water to eliminate any possible impurities. Finally, the solid product was kept in a vacuum oven overnight at  $60 \text{ }^\circ\text{C}$  for drying. In a similar fashion,  $\text{W}_{18}\text{O}_{49}$ , Ru  $\text{W}_{18}\text{O}_{49}$ -2.5%, and Ru- $\text{W}_{18}\text{O}_{49}$ -7.5% were all fabricated utilizing the same synthetic approach with adding various amounts of  $\text{RuCl}_3 \cdot 6\text{H}_2\text{O}$  (0 g, 0 mmol), (0.0065 g, 0.02 mmol), and (0.02 g, 0.063 mmol), respectively, in tungsten (VI) chloride solution during the synthesis process. Note that 2.5%, 5%, 7.5% are the weight percents of  $\text{RuCl}_3 \cdot 6\text{H}_2\text{O}$  in the mixture solution of tungsten (VI) chloride and ruthenium (III) chloride in each time.

### 1.3. Physical characterizations

The X-ray diffraction (XRD) patterns were obtained using a Rigaku D/max 2500 X-ray diffractometer with  $\text{Cu K}\alpha$  radiation (40 kV, 30 mA,  $\lambda=1.5418 \text{ \AA}$ ) at a  $10^\circ \text{ min}^{-1}$  scan rate in the range of  $2\theta$  from 5 to 90 degrees. The surface morphology of the samples was characterized utilizing a scanning electron microscope (SEM, Zeiss SUPRA55) with an accelerating voltage of 5 kV, while transmission electron microscope (TEM) images were obtained with a JEOL JEM 2100. High resolution TEM (HR-TEM) analysis was carried out on an FEI Titan G3i-300 KeV FEG-TEM (field emission gun transmission electron microscope) operating at a voltage of 300 kV. Energy-dispersive X-ray spectroscopy (EDS) data and elemental mapping of Ru- $\text{W}_{18}\text{O}_{49}$  were acquired using High Angle Annular Dark Field-Scanning Transmission Electron Microscopy (HAADF-STEM). X-ray photoelectron spectra (XPS) were collected using an ESCALAB 250 and the XPS data were analyzed using the CasaXPS software. Calibration of the binding energies was done using C 1s (284.8 eV). The weight percentages of the elements were measured by inductively coupled plasma optical emission spectrometry (ICP-OES) using an, iCAP7400, from, Thermo Fisher).

### 1.4. Electrochemical measurements

All electrochemical measurements have been carried out using a standard three-electrode electrochemical cell controlled by a CHI760D electrochemical workstation (CH Instruments, Shanghai, China). The samples'

catalytic activity was assessed in a solution of 0.5 M H<sub>2</sub>SO<sub>4</sub>. The as-prepared catalysts, or commercial samples-coated carbon fiber paper, graphite rod, and Hg/HgCl<sub>2</sub> electrode were utilized as the working, counter, and reference electrode respectively. The catalyst's homogenous ink was created by ultrasonically dispersing the catalyst in 0.98 ml ethanol including 20 µl 5% Nafion solution. To assess the HER activity of the as-created catalysts or commercial samples, the ink was sprayed onto a carbon fiber paper with area of 1 cm<sup>2</sup> to form a catalyst thin film. The mass loading of catalysts on CFP was 1 mg cm<sup>-2</sup> for the as-prepared catalysts, whereas 0.5 mg cm<sup>-2</sup> for commercial 20 wt.%- Pt /C and 5 wt.%- Ru /C. All the electrochemical experiments were conducted at ambient temperature after stabilizing the catalyst by several CV cycles. The LSV curves for the as-created catalysts, or commercial samples were then recorded at a 5 mV/s scan rate in the range between 0 to -1 V vs. Hg/HgCl<sub>2</sub>. The equation of E(RHE) = E(Hg/HgCl<sub>2</sub>) + 0.059 pH + 0.24 was used to adjust the potentials to reversible hydrogen electrode (RHE). All polarization curves were corrected with an ohmic potential drop (iR) originating from the solution resistance determined by electrochemical impedance spectroscopy (EIS). In order to quantify the system resistance, the electrochemical impedance spectroscopy was acquired by AC impedance spectroscopy in a solution of 0.5 M H<sub>2</sub>SO<sub>4</sub> at an open circuit voltage from 10<sup>5</sup> Hz to 0.1 Hz with an AC voltage of 5 mV. In a three-electrode system with a reference electrode of Hg/HgCl<sub>2</sub>, a counter electrode of graphite rod, and the as-prepared material as the working electrode, the chronopotentiometry (CP) test was used to investigate the catalyst's long-term durability at a constant current density of 100 mA cm<sup>-2</sup>. The acquired CP test results were shown without iR correction and in their raw form. As a result of fitting the LSV curves at a low overpotential to the Tafel equation (1), the Tafel slopes were calculated.

$$\eta = a + b \log j \quad (1)$$

Where  $\eta$  represents the overpotential (V),  $b$  denotes the Tafel slope (mV dec<sup>-1</sup>),  $j$  signifies the current density (mA cm<sup>-2</sup>), and  $a$  is the constant. The electrochemical double-layer capacitance ( $C_{dl}$ ) was calculated via conducting cyclic voltammetry (CV) within a non-faradic potential range at various scan rates (10-100 mV s<sup>-1</sup>). Then, the capacitive currents at the central voltage against scan rates were fitted to obtain  $C_{dl}$ . Equation 2 was used to determine the Electrochemical active surface area (ECSA) of a catalyst sample based on its double-layer capacitance.

$$ECSA = C_{dl} / C_s \quad (2)$$

Where  $C_s$  represents the sample's specific capacitance. The mass activity (A g<sup>-1</sup>) was evaluated according to the following equation: -

$$\text{Mass activity} = j / m \quad (3)$$

Where,  $m$  is the loading amount of Ru on the electrode (mg cm<sup>-2</sup>), and  $j$  represents the obtained current density (mA cm<sup>-2</sup>) from LSV curves at definite overpotential. The turnover frequency (TOF, s<sup>-1</sup>) was calculated with the following equation

$$\text{TOF} = j \cdot A / 2 \cdot n \cdot F \quad (4)$$

Where,  $j$  is the measured current density (A cm<sup>-2</sup>) from LSV polarization curves at a definite overpotential,  $A$  is the geometric area of the working carbon fiber paper (1 cm<sup>2</sup>),  $F$  is the Faraday constant (96485 C·mol<sup>-1</sup>), and  $n$  refers to the number of moles of Ru that are deposited on the electrode. The as-created sample's decay was determined by dividing the amount of decay in CP or LSV curves in comparison to pristine LSV curve by time.

### 1.5. Computational details

DFT calculations were performed by the Vienna Ab-initio Simulation Package (VASP) with the projector augmented wave method [1, 2]. For the exchange and correlation energy density functions, the Perdew-Burke-Ernzerhof (PBE) generalized gradient approximation (GGA) was adopted [3, 4]. For the cutoff energy, the 450 eV was chosen, which was consistent with previous work [5]. In order to improve the accuracy of model calculation, the DFT+U calculation method was used to describe the correlation of 3d transition metal system. The U values of DFT+U are tested using the linear response approximation method, and the calculated results show that the U values of W and Ru are 3.70 and 4.81 eV, respectively. The 3×3×3 and 2×2×1 Monkhorst-Pack type k-point sampling was chosen to optimize bulk structure and slab model [6]. Choosing 0.01 eV/Å and 10–4 eV as the convergence criteria of force and energy, respectively [7]. Bader charge analysis used to obtain the charge W, spin calculation of adsorbed species was also performed [8].

## 2. The proposed mechanism for W<sub>18</sub>O<sub>49</sub> synthesis

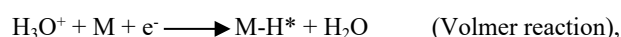
The proposed mechanism for W<sub>18</sub>O<sub>49</sub> synthesis and the unexpected morphological transformation upon adding RuCl<sub>3</sub>·6H<sub>2</sub>O is as follows. Initially, WCl<sub>6</sub> reacts with C<sub>2</sub>H<sub>5</sub>OH, producing C<sub>2</sub>H<sub>5</sub>OWCl<sub>5</sub> and HCl (**Equation 1, Scheme S1**). An etherification reaction occurs between two molecules of C<sub>2</sub>H<sub>5</sub>OH, generating a molecule of water (**Equation 2, Scheme S1**). Subsequently, the complex of C<sub>2</sub>H<sub>5</sub>OWCl<sub>5</sub> with the H<sub>2</sub>O generated from the etherification reaction to form W<sub>18</sub>O<sub>49</sub> (**Equation 3, Scheme S1**) [9].

Typically, W<sub>18</sub>O<sub>49</sub> crystal nuclei mainly grow into uniform nanorods. However, upon the addition of RuCl<sub>3</sub>, a substantial change in the sample's color, from blue to green, is observed along with an unexpected morphological transformation from radial nanorods to urchin-like nanospheres assembled from these nanorods. This indicates that the minor doping with Ru is critical for the appearance of this unique morphology. Ru ions are believed to adsorb onto specific crystal faces of the W<sub>18</sub>O<sub>49</sub> crystals, thereby modulating the growth kinetics and surface interactions. This adsorption could lead to anisotropic growth, promoting the self-assembly of nanorods into urchin-like nanospheres during the hydrothermal reaction to minimize overall surface energy. Additionally, Ru ions may facilitate the formation of bridging structures or influence electrostatic interactions between nanorods, further stabilizing the urchin-like morphology (**Scheme S1**).

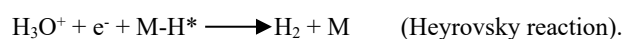
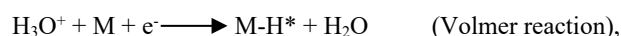
## 3. HER mechanism based on Tafel slope value

The reaction mechanisms include Volmer-Tafel and Volmer-Heyrovsky, distinguished by the value of Tafel slope. When the value of Tafel slope is larger than 40 mV dec<sup>-1</sup>, the reaction path in acidic HER is Volmer-Heyrovsky, otherwise is Volmer-Tafel. In our work, the Tafel slopes of W<sub>18</sub>O<sub>49</sub> and Ru-W<sub>18</sub>O<sub>49</sub>-2.5% are 320.6 and 81.2 mV dec<sup>-1</sup>, larger than 40 mV dec<sup>-1</sup>, indicating that the HER follows the Volmer-Heyrovsky pathway. However, the Tafel slope value of Ru-W<sub>18</sub>O<sub>49</sub>-5% and Ru-W<sub>18</sub>O<sub>49</sub>-7.5% are 33.8 and 37.8 mV dec<sup>-1</sup>, falling in the range of (30-40) mV dec<sup>-1</sup>, indicating that the HER follows the Volmer-Tafel pathway (Figure S6).

Volmer-Tafel mechanism



Volmer-Heyrovsky mechanism



#### 4. Determination of active sites

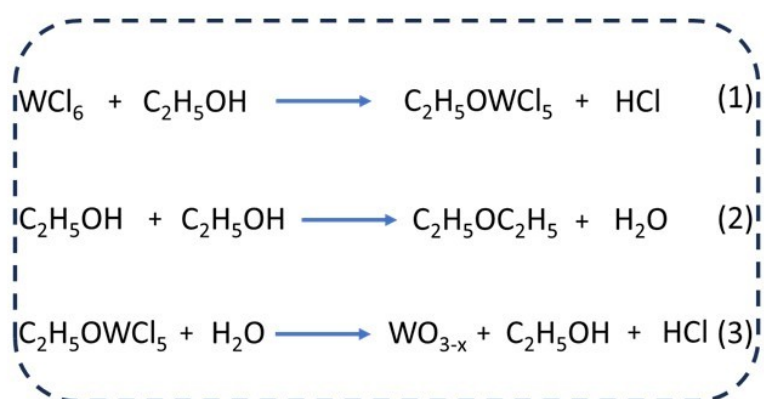
The hydrogen adsorption energy is widely recognized as a key descriptor for predicting catalyst performance in HER. To determine the active site of the catalyst for HER, the hydrogen adsorption energy on different possible active sites of Ru-W<sub>18</sub>O<sub>49</sub>-5% sample are calculated by DFT in Figure S12. Four active sites are labeled on the top view model: sites (1 and 4) are occupied by W<sup>5+</sup>, far from Ru dopant (site 3) with different distances and site 2 is occupied by W<sup>6+</sup>. By comparison, the hydrogen adsorption energy of site 1 (0.5162 eV) is greatest, not conducive to hydrogen absorption, and that of site 3 (0.0036 eV) is closest to zero with optimal binding strength. Therefore, site 3 with Ru dopant is considered as the active site for HER.

#### 5. Characterizations after stability test

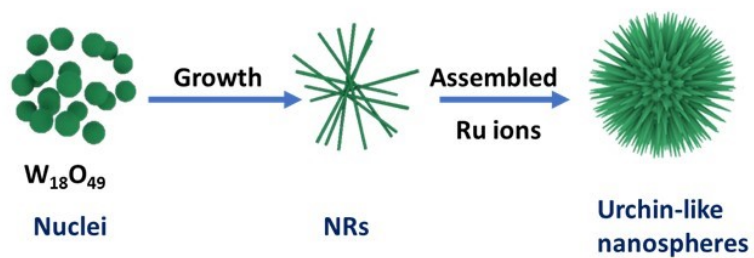
To gain a detailed understanding of the structural and compositional changes in Ru-W<sub>18</sub>O<sub>49</sub>-5% after the chronopotentiometry (CP) test at 100 mA cm<sup>-2</sup>, various microscopic, spectroscopic, and diffraction techniques were employed. These analyses aimed to elucidate the nature of the active sites and their correlation with the structure and catalytic activity. The XRD (**Fig. S9**) and the SAED pattern (**Fig. S10**) of Ru-W<sub>18</sub>O<sub>49</sub>-5% after durability test showed no significant changes compared to those before the HER operation, indicating the original crystal structure was maintained after the long-term stability test. In addition, the EDX analysis confirmed the presence of Ru, W, and O elements in the sample post stability test (**Fig. S10**). High-angle annular dark field-scanning transmission electron microscopy (HAADF-STEM) at a scale of 10 nm show that Ru, W, and O elements are still highly dispersed and evenly distributed throughout the sample (**Fig. S10**). This uniform elemental dispersion further supports the excellent structural stability of Ru-W<sub>18</sub>O<sub>49</sub>-5% during HER process.

However, SEM and TEM images (**Fig. S9**) showed a rupture and disappearance of radial nanorods at the nanosphere margins of Ru-W<sub>18</sub>O<sub>49</sub>-5% after CP test. This morphology change suggests a reduction in the exposure of active sites, potential contributing to the observed performance decline over long time operation. In addition, it is clarified from XPS data that the proportion of W(V), and oxygen vacancy increased compared to the pre-HER conditions (**Table S2, S3, and Figure S11**). Furthermore, the proportion of Ru<sup>4+</sup> declined, suggesting the catalyst underwent some reduction during the durability test (**Figure S11**). Also, the increased quantity of OH groups was detected (**Figure S11, and Table S3**), indicating improved hydrophilicity, which is beneficial for accelerating the HER reaction rate.

A



B



**Scheme S1.** Synthesis of urchin-like Ru- $\text{W}_{18}\text{O}_{49}$  nanospheres. (A) The proposed synthesis mechanism of  $\text{W}_{18}\text{O}_{49}$ , (B) The schematic diagram of the formation mechanism of urchin-like Ru - $\text{W}_{18}\text{O}_{49}$  nanospheres.

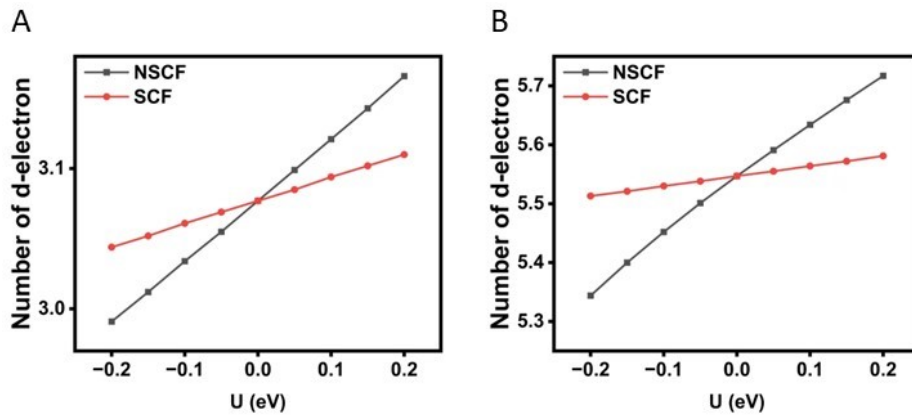


**Figure S1.** Linear response curves for A) W and B) Ru, where the black and red lines represent the corresponding number of d-electrons calculated without U-values for non-self-consistent and self-consistent calculations, respectively.

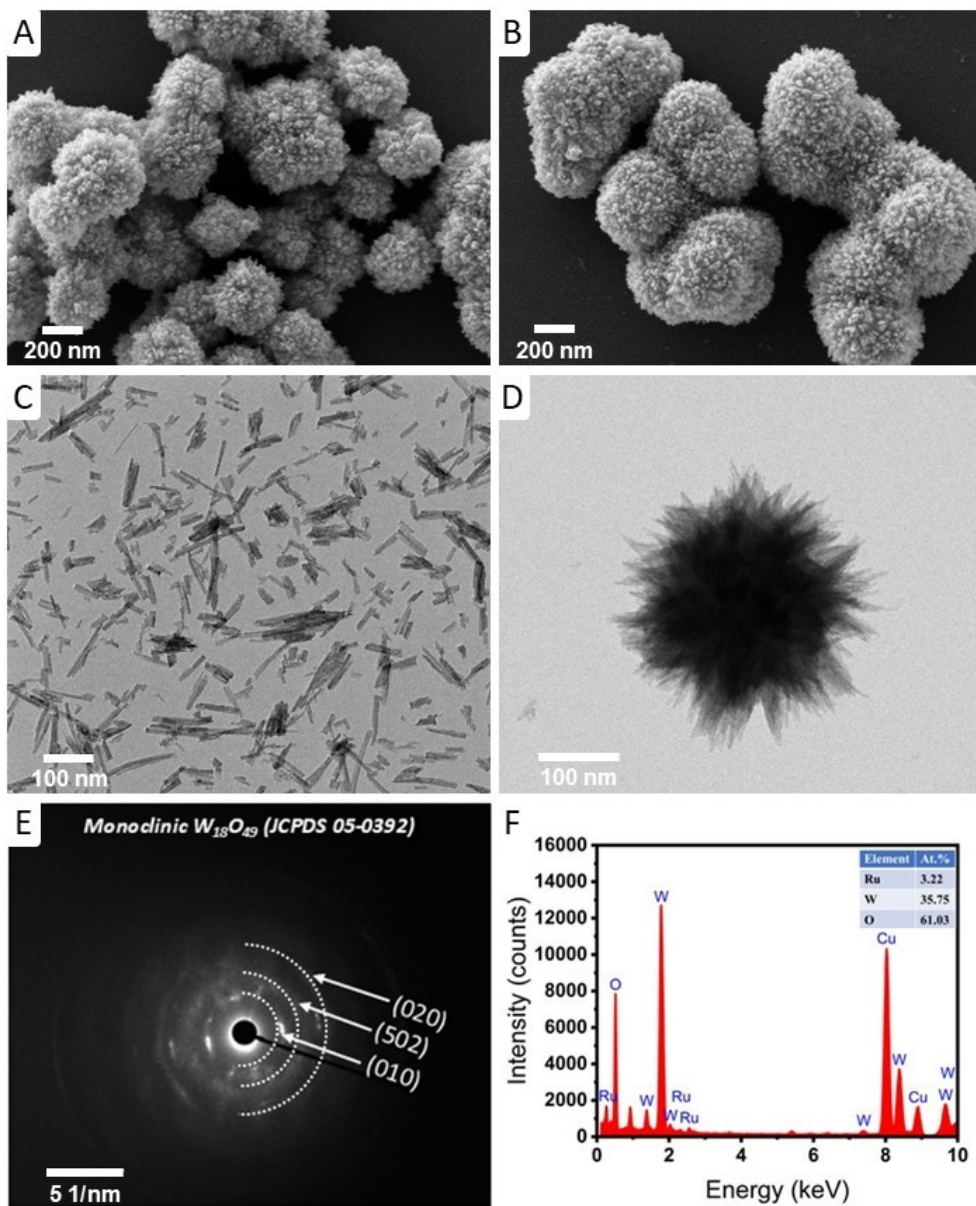


**Figure S2.** SEM images for (A) Ru-W<sub>18</sub>O<sub>49</sub>-2.5%, (B) Ru-W<sub>18</sub>O<sub>49</sub>-7.5%. TEM images for (C) W<sub>18</sub>O<sub>49</sub>, (D) Ru-W<sub>18</sub>O<sub>49</sub>-5%. (E) The selected area electron diffraction (SAED) pattern, (F) The EDX analysis of Ru-W<sub>18</sub>O<sub>49</sub>-5%. The EDX analysis confirms the presence of Ru, W, and O and the peaks for copper can be unambiguously correlated to the TEM grid (carbon film on 300 mesh Cu-grid).

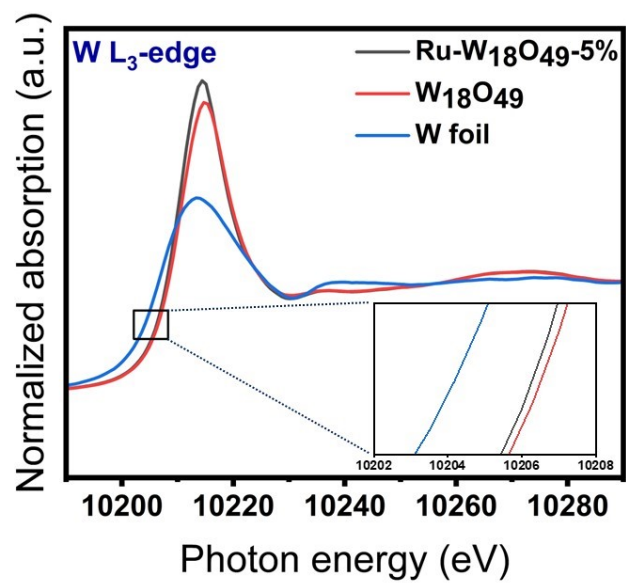


**Figure S3.** W L<sub>3</sub>-edge XANES spectra of W<sub>18</sub>O<sub>49</sub> and Ru-W<sub>18</sub>O<sub>49</sub>-5% with W foil



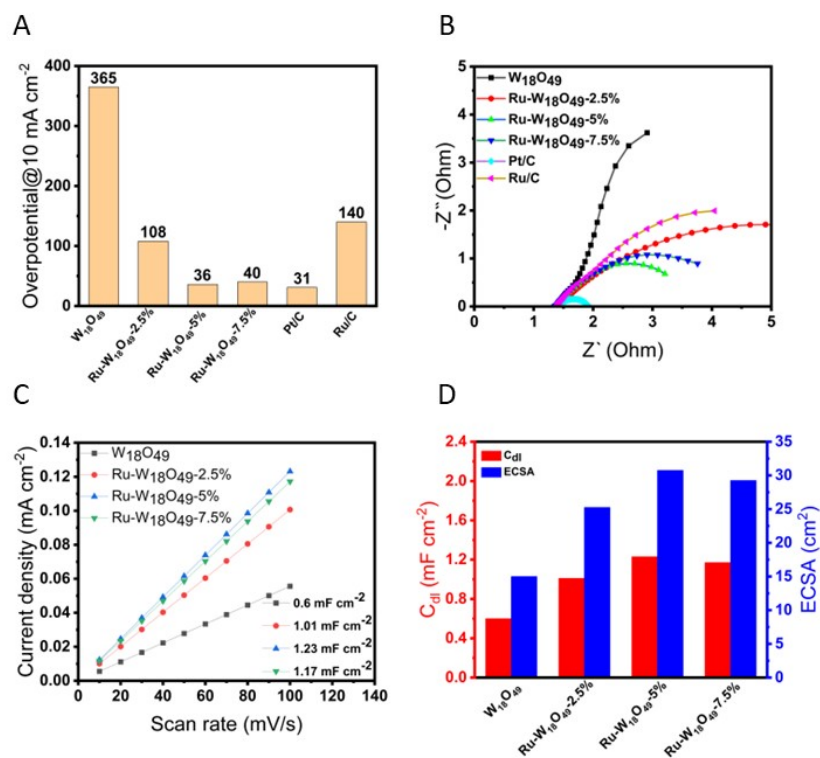


**Figure S5.** (A) comparison of the as-prepared samples with commercial samples according to the value of overpotential @10 mA cm<sup>-2</sup>, (B) Nyquist plot of the as-prepared samples and commercial samples attained from EIS, (C) The electrochemical double-layer capacitances, C<sub>dl</sub> (D) graph shows the values of C<sub>dl</sub> and their corresponding ECSA values.

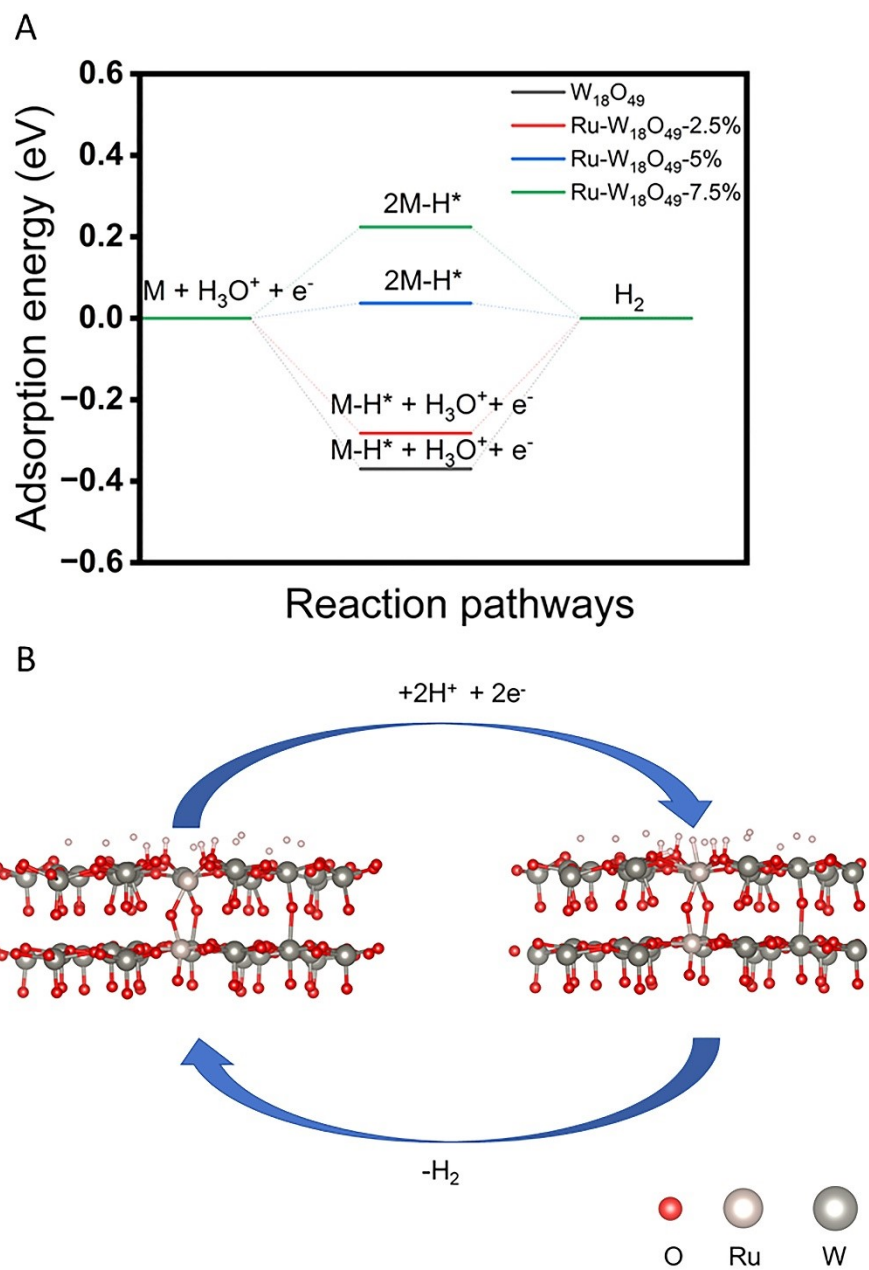


**Figure S6.** (A) HER reaction Pathway and step diagram (B) Structural diagram of the Tafel reaction intermediate in  $Ru-W_{18}O_{49}-5\%$  HER with 60% H coverage.

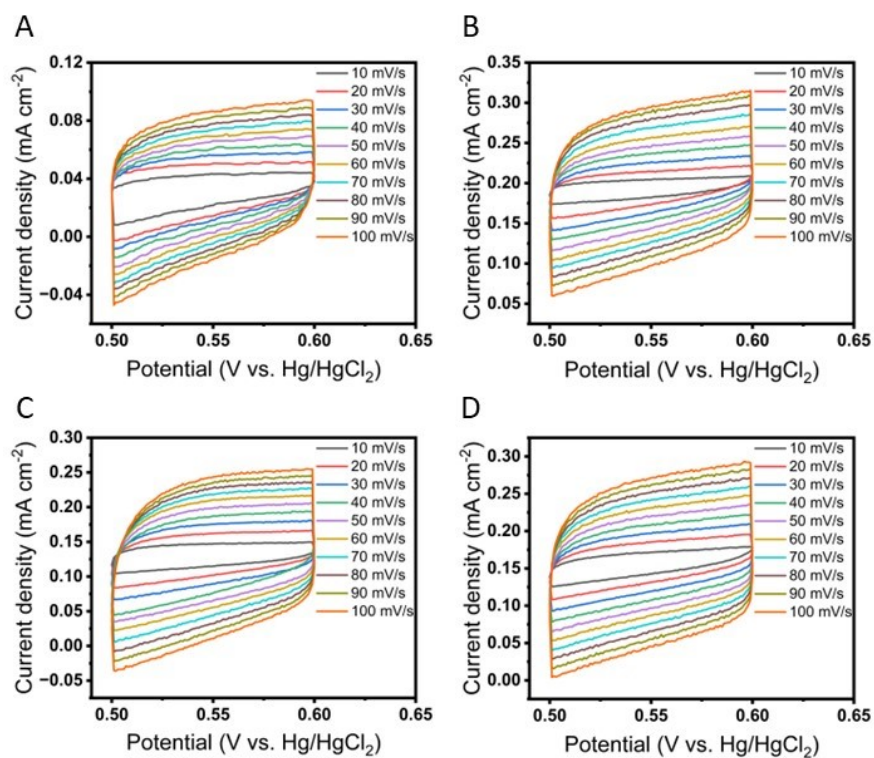


**Figure S7.** CV curves for (A)  $W_{18}O_{49}$ , (B) Ru- $W_{18}O_{49}$ -2.5%, (C) Ru- $W_{18}O_{49}$ -5%, (D) Ru- $W_{18}O_{49}$ -7.5%, from 0.5 to 0.6 V vs. Hg/HgCl<sub>2</sub> at a scan rate from 10 to 100 mV/s.

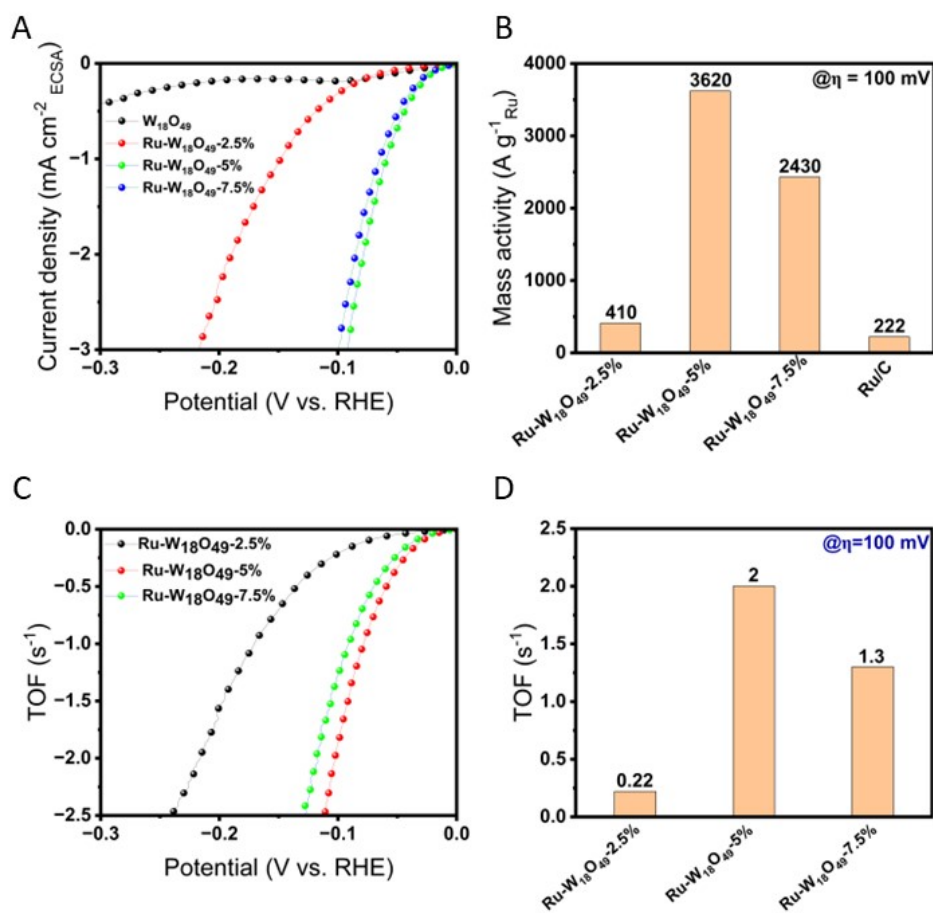


**Figure S8.** (A) Normalized polarization curves by ECSA of W<sub>18</sub>O<sub>49</sub> and Ru-W<sub>18</sub>O<sub>49</sub> samples, (B) comparison the as-prepared samples according to their values of mass activity at 0.1 V vs. RHE, (C) TOF of the as-prepared Ru-W<sub>18</sub>O<sub>49</sub> samples, (D) comparison TOF values of the as-prepared Ru-W<sub>18</sub>O<sub>49</sub> samples at 0.1 V vs. RHE.

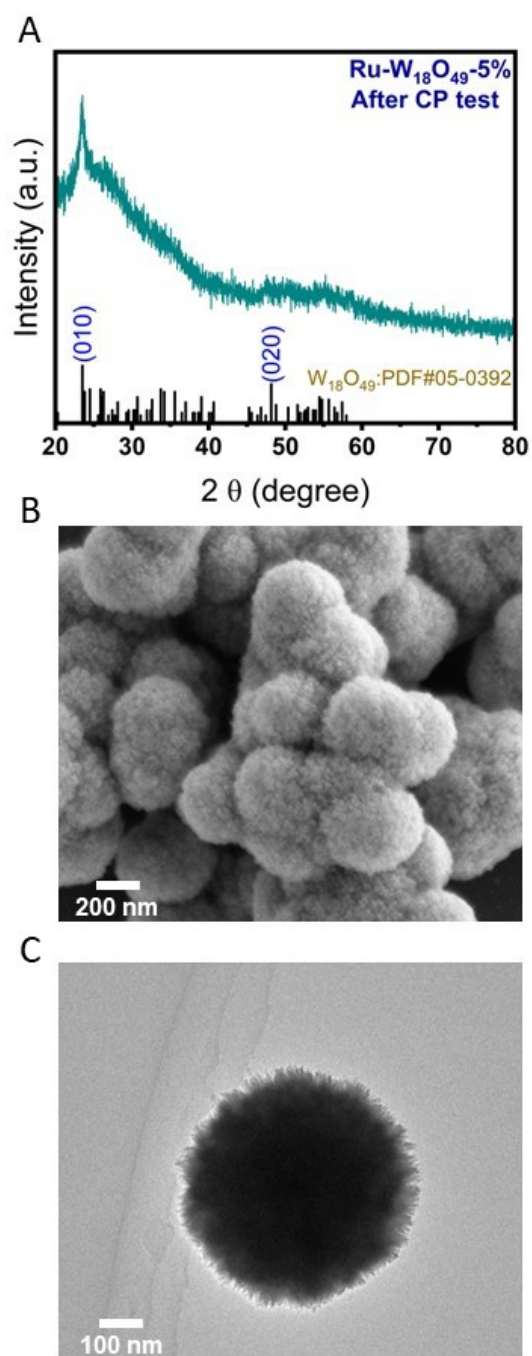


**Figure S9.** (A) XRD, (B) SEM, (C) TEM of Ru-W<sub>18</sub>O<sub>49</sub>-5% after CP test.

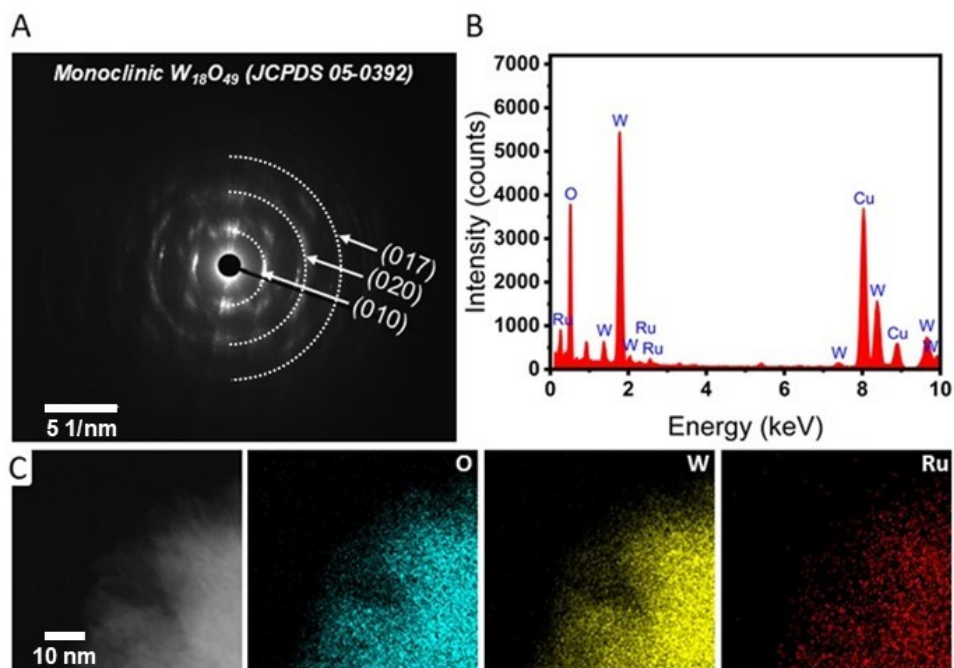


**Figure S10.** (A) SAED pattern, (B) The EDX analysis confirming the presence of O, W, and Ru elements. The peaks for copper can be unambiguously correlated to the TEM grid (carbon film on 300 mesh Cu-grid), (C) Elemental mapping at a 10 nm scale by HAADF-STEM of Ru- $W_{18}O_{49}$ -5% after CP test.

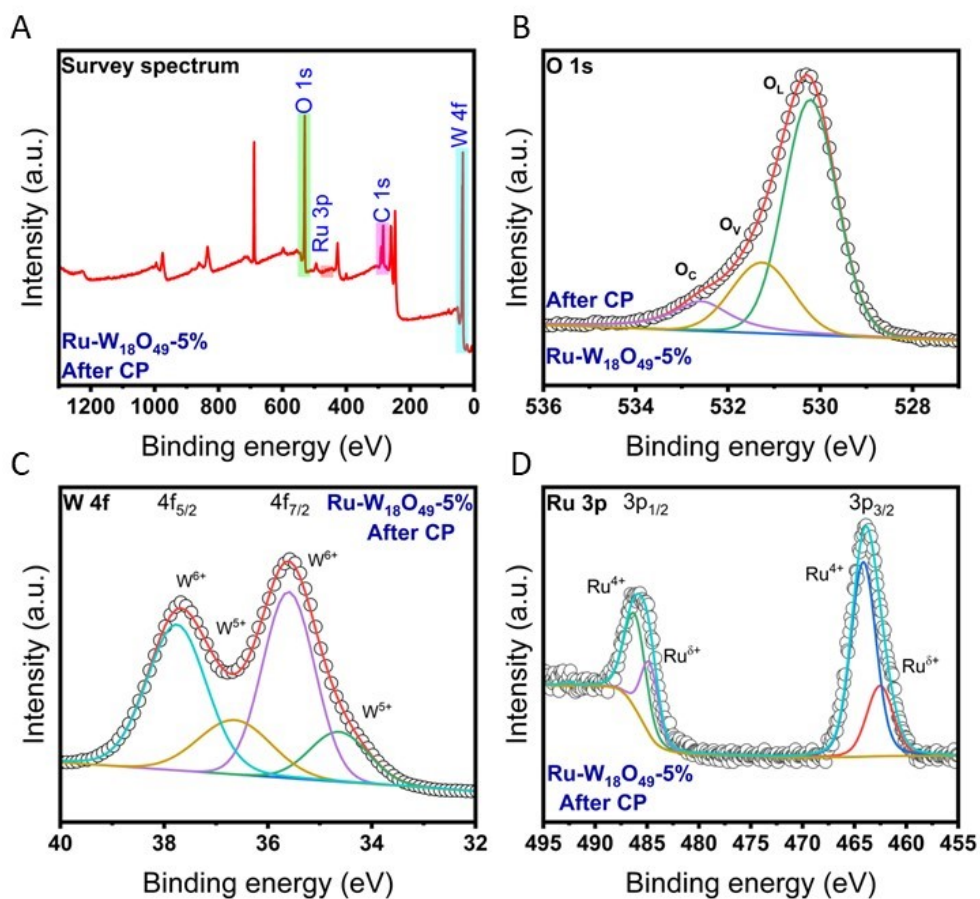
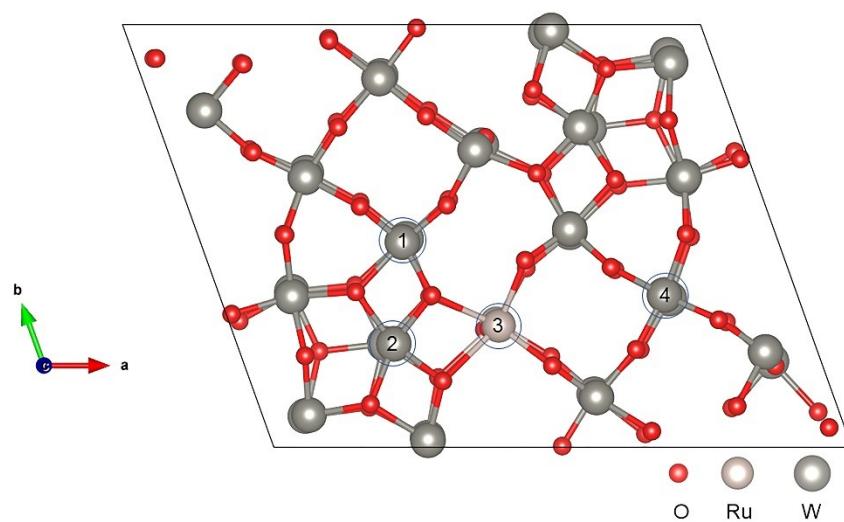


**Figure S11.** XPS data of Ru-W<sub>18</sub>O<sub>49</sub>-5% after CP test. (A) The XPS survey spectrum (B) The high-resolution deconvoluted of O 1s (C) The high-resolution deconvoluted of W 4f (D) The high-resolution deconvoluted of Ru 3p XPS spectra.



Sites	Hydrogen adsorption energy/eV
1	0.51616665
2	0.17326804
3	0.0036207
4	0.13311847

**Figure S12.** Different reaction sites and their hydrogen ion adsorption energy.

**Table S1.** Ru wt.% and W wt.% determined by inductively coupled plasma analysis spectrometry (ICP) technique in the as-prepared samples.

Catalyst name	Wt. % of Ru	Wt. % of W
Ru-W <sub>18</sub> O <sub>49</sub> -2.5%	1.965	79.26
Ru-W <sub>18</sub> O <sub>49</sub> -5%	3.225	78.235
Ru-W <sub>18</sub> O <sub>49</sub> -7.5%	3.655	77.895

**Table S2.** Summarized data from W 4f XPS spectra of different samples.

Samples	Valence state	Binding energy (eV)		Concentration (at. %)
		W4f <sub>7/2</sub>	W4f <sub>5/2</sub>	
W <sub>18</sub> O <sub>49</sub>	W <sup>5+</sup>	34.75	36.77	20%
	W <sup>6+</sup>	35.73	37.89	80%
Ru-W <sub>18</sub> O <sub>49</sub> -5%	W <sup>5+</sup>	34.65	36.67	26%
	W <sup>6+</sup>	35.63	37.79	74%
Ru-W <sub>18</sub> O <sub>49</sub> -5% (After CP test)	W <sup>5+</sup>	34.63	36.64	27%
	W <sup>6+</sup>	35.6	37.76	73%

**Table S3.** the proportion of oxygen species tested by XPS.

Samples	Lattice oxygen	Oxygen vacancy	Adsorbed oxygen
W <sub>18</sub> O <sub>49</sub>	71.8	21.9%	6.3%
Ru-W <sub>18</sub> O <sub>49</sub> -5%	71.7	21.5%	6.8%
Ru-W <sub>18</sub> O <sub>49</sub> -5% after CP test	64	23%	13%

**Table S4.** Summary of recently reported representative HER electrocatalysts based on Ru in acidic electrolyte.  $\eta$  is the overpotential

Catalysts	Loading amount	$\eta_{10}$ (mV)	Tafel slope (mV dec <sup>-1</sup> )	Ref.
<b>Ru-W<sub>18</sub>O<sub>49</sub></b>	<b>0.032 mg<sub>Ru</sub> cm<sup>-2</sup></b>	<b>36</b>	<b>33.8</b>	<b>This work</b>
RuP <sub>2</sub> @NPC	0.233 mg <sub>Ru</sub> cm <sup>-2</sup>	38	38	[10]
Ru-HPC	0.2 mg cm <sup>-2</sup>	61.6	66.8	[11]
Ru@CN-0.16	0.26 mg cm <sup>-2</sup>	126	N/A	[12]
NiRu@N-C	0.273 mg cm <sup>-2</sup>	50	36	[13]
Ru-MoO <sub>2</sub>	0.57 mg cm <sup>-2</sup>	55	44	[14]
Cu <sub>2-x</sub> S@Ru nanoplates	0.23 mg cm <sup>-2</sup>	129	51	[15]
Ni@Ni <sub>2</sub> P-Ru	0.286 mg cm <sup>-2</sup>	51	35	[16]
Hcp-Ru@NC	0.28 mg cm <sup>-2</sup>	27.5	37	[17]
1D-RuO <sub>2</sub> -CN <sub>x</sub>	0.171 mg <sub>RuO2</sub> cm <sup>-2</sup>	93	40	[18]
Ru@C <sub>2</sub> N	0.285 mg cm <sup>-2</sup>	13.5	30	[19]
s-RuS <sub>2</sub> /S-rGO	0.176 mg <sub>Ru</sub> cm <sup>-2</sup>	69	64	[20]
Ru@GnP	0.14 mg <sub>Ru</sub> cm <sup>-2</sup>	13	30	[21]
C <sub>3</sub> N <sub>4</sub> -Ru-F	0.153 mg cm <sup>-2</sup>	140	57	[22]
Ru@MWCNT	0.7 mg cm <sup>-2</sup>	13	27	[23]
Ru <sub>0.10</sub> @2H-MoS <sub>2</sub>	0.02 mg cm <sup>-2</sup>	168	77.5	[24]
Ru/WO <sub>3</sub> -V <sub>O</sub>	0.28 mg cm <sup>-2</sup>	65	66.3	[25]

## References

- [1] G. Kresse, J. Furthmüller, *Comput. Mater. Sci.*, 1996, **6**, 15-50.
- [2] G. Kresse, J. Furthmüller, *Phys. Rev. B.*, 1996, **54**, 11169.
- [3] P.E. Blöchl, *Phys. Rev. B.*, 1994, **50**, 17953.
- [4] G. Kresse, D. Joubert, *Phys. Rev. B.*, 1999, **59**, 1758.
- [5] J. Rossmeisl, A. Logadottir, J.K. Nørskov, *Chem. Phys.*, 2005, **319**, 178-184.
- [6] D. Chadi, *Phys. Rev. B.*, 1977, **16**, 790.
- [7] G. Henkelman, A. Arnaldsson, H. Jónsson, *Comput. Mater. Sci.*, 2006, **36**, 354-360.
- [8] Z. Cai, D. Zhou, M. Wang, S.M. Bak, Y. Wu, Z. Wu, Y. Tian, X. Xiong, Y. Li, W. Liu, *Angew. Chem.*, 2018, **130**, 9536-9540.
- [9] R. Zhou, X. Lin, D. Xue, F. Zong, J. Zhang, X. Duan, Q. Li, T. Wang, *Sens. Actuators B: Chem.*, 2018, **260**, 900-907.
- [10] Z. Pu, I.S. Amiinu, Z. Kou, W. Li, S. Mu, *Angew. Chem. Int. Ed.*, 2017, **56**, 11559-11564.

- [11] T. Qiu, Z. Liang, W. Guo, S. Gao, C. Qu, H. Tabassum, H. Zhang, B. Zhu, R. Zou, Y. Shao-Horn, *Nano Energy*, 2019, **58**, 1-10.
- [12] J. Wang, Z. Wei, S. Mao, H. Li, Y. Wang, *Energy Environ. Sci.*, 2018, **11**, 800-806.
- [13] Y. Xu, S. Yin, C. Li, K. Deng, H. Xue, X. Li, H. Wang, L. Wang, *J. Mater. Chem. A*, 2018, **6**, 1376-1381.
- [14] P. Jiang, Y. Yang, R. Shi, G. Xia, J. Chen, J. Su, Q. Chen, *J. Mater. Chem. A*, 2017, **5**, 5475-5485.
- [15] D. Yoon, J. Lee, B. Seo, B. Kim, H. Baik, S.H. Joo, K. Lee, *Small*, 2017, **13**, 1700052.
- [16] Y. Liu, S. Liu, Y. Wang, Q. Zhang, L. Gu, S. Zhao, D. Xu, Y. Li, J. Bao, Z. Dai, *J. Am. Chem. Soc.*, 2018, **140**, 2731-2734.
- [17] Y. Li, L.A. Zhang, Y. Qin, F. Chu, Y. Kong, Y. Tao, Y. Li, Y. Bu, D. Ding, M. Liu, *ACS Catal.*, 2018, **8**, 5714-5720.
- [18] T. Bhowmik, M.K. Kundu, S. Barman, *ACS Appl. Mater. Interfaces*, 2016, **8**, 28678-28688.
- [19] J. Mahmood, F. Li, S.-M. Jung, M.S. Okyay, I. Ahmad, S.-J. Kim, N. Park, H.Y. Jeong, J.-B. Baek, *Nat. Nanotechnol.*, 2017, **12**, 441-446.
- [20] J. Yu, Y. Guo, S. Miao, M. Ni, W. Zhou, Z. Shao, *ACS Appl. Mater. Interfaces*, 2018, **10**, 34098-34107.
- [21] F. Li, G.F. Han, H.J. Noh, I. Ahmad, I.Y. Jeon, J.B. Baek, *Adv. Mater.*, 2018, **30**, 1803676.
- [22] Y. Peng, B. Lu, L. Chen, N. Wang, J.E. Lu, Y. Ping, S. Chen, *J. Mater. Chem. A*, 2017, **5**, 18261-18269.
- [23] D.H. Kweon, M.S. Okyay, S.-J. Kim, J.-P. Jeon, H.-J. Noh, N. Park, J. Mahmood, J.-B. Baek, *Nat. Commun.*, 2020, **11**, 1278.
- [24] J. Wang, W. Fang, Y. Hu, Y. Zhang, J. Dang, Y. Wu, B. Chen, H. Zhao, Z. Li, *Appl. Catal., B*, 2021, **298**, 120490.
- [25] J. Cai, W. Zhang, Y. Liu, R. Shen, X. Xie, W. Tian, X. Zhang, J. Ding, Y. Liu, B. Li, *Appl. Catal., B*, 2024, **343**, 123502.